



1 **Molecular insight into aqueous-phase photolysis and photooxidation**
2 **of water-soluble organic matter emitted from biomass burning and**
3 **coal combustion**

4 Tao Cao¹, Cuncun Xu^{1,2}, Hao Chen^{1,2}, Jianzhong Song^{1,3,*}, Jun Li^{1,3}, Haiyan Song⁴,
5 Bin Jiang^{1,3}, Yin Zhong^{1,3}, Ping'an Peng^{1,2,3}

6 ¹State Key Laboratory of Advanced Environmental Technology and Guangdong
7 Provincial Key Laboratory of Environmental Protection and Resources Utilization,
8 Guangzhou Institute of Geochemistry, Chinese Academy of Sciences, Guangzhou
9 510640, China

10 ²University of Chinese Academy of Sciences, Beijing 100049, China

11 ³Guangdong-Hong Kong-Macao Joint Laboratory for Environmental Pollution and
12 Control, Guangzhou 510640, China

13 ⁴School of Chemistry, South China Normal University, Universities Town,
14 Guangzhou 510006, China

15

16 *Correspondence to: Jianzhong Song, E-mail: songjzh@gig.ac.cn.

17

18



19 **Abstract**

20 Biomass and coal combustion represent substantial contributors to atmospheric
21 water-soluble organic matter (WSOM). It experienced intense photochemical
22 oxidation once entered atmospheric environment, but the resulting changes in WSOM
23 are largely unclear. This study examines the changes in the optical properties,
24 fluorophores, and molecular composition of WSOM derived from the combustion of
25 biomass (specifically rice straw, RS) and coal (from Yulin, YL) during aqueous
26 photolysis and hydroxyl radical (OH) photooxidation. The results indicate that
27 photochemical aging induces distinct changes in the light-absorbing properties of RS
28 and YL WSOM, characterized by pronounced photobleaching in RS WSOM and
29 photoenhancement in YL WSOM. Additionally, more pronounced alterations were
30 observed during OH photooxidation than direct photolysis, for both RS and YL
31 WSOM. Furthermore, a greater proportion of molecules in both RS (61.6%) and YL
32 (65.0%) WSOM were degraded during OH photooxidation compared to photolysis
33 (14.9% and 23.1%, respectively), resulting in products with larger molecular weight
34 and higher oxidation levels, including tannin-like substances and newly formed black
35 carbon-like compounds, whereas the products of photolysis were characterized by
36 relative minor alteration. These findings provide new insights into the photochemical
37 evolution of combustion-derived WSOM and help to predict its effects in
38 environmental and climate changes.

39

40



41 **1. Introduction**

42 Water-soluble organic matter (WSOM) consists of diverse array of polar organic
43 species, which is ubiquitous in atmospheric aerosols, cloud, fog, and rain waters (Sun
44 et al., 2023; Wang et al., 2019). WSOM can not only alter the hygroscopicity and
45 surface tension of aerosol, influence the formation of cloud condensation nuclei, but
46 also has significant effects on the radiative forcing of aerosols, thereby playing crucial
47 roles in atmospheric environment and climate change (Sun et al., 2011; Chen et al.,
48 2019; Lee et al., 2022). Due to its high reactivity, WSOM also contributes to
49 atmospheric chemistry and the formation of organic aerosols. Moreover, WSOM has
50 the potential to catalyze the generation of reactive oxygen species, posing adverse
51 impacts on human health (Bhattu et al., 2024; Bates et al., 2019).

52 Multiple sources of WSOM have been identified, including primary emissions
53 from biomass burning (BB), coal combustion (CC), vehicular emissions, and
54 secondary formation through the photochemical transformation of volatile organic
55 compounds (Tang et al., 2020; Jiang et al., 2023; Cao et al., 2023). Among these
56 sources, BB has been recognized as a significant contributor to atmospheric WSOM
57 in numerous regions, including East Asia, Southeastern Asia (Liu et al., 2021; Zheng
58 et al., 2017), the Amazon rainforest (Malavelle et al., 2019), and North America
59 (Gallo et al., 2023; Ceamanos et al., 2023). Furthermore, domestic coal combustion
60 also serves as a crucial primary source of atmospheric WSOM in northern China and
61 India (Bikkina et al., 2020; Liu et al., 2022), as well as in Poland (Casotto et al., 2023).
62 It is important to note that the combustion-derived primary WSOM experiences



63 considerable aging upon entering the atmosphere (Sumlin et al., 2017; Schnitzler et al.,
64 2022). For instance, studies have reported a marked decrease in the light absorption of
65 water-soluble brown carbon (BrC) during transport over distances exceeding 6000 km
66 from the Indo-Gangetic Plain to the Himalayan region (Dasari et al., 2019; Choudhary
67 et al., 2022). Additionally, observations of wildfire plumes in North America have
68 demonstrated a reduction in the mass absorption coefficient as the plume ages (Bali et
69 al., 2024). Nonetheless, the concentrations, light absorption properties, and chemical
70 characteristics of WSOM undergo significant alterations throughout the atmospheric
71 aging process.

72 Field and laboratory studies demonstrated that aqueous photochemical processes
73 including direct photolysis and secondary photochemistry involving with oxidants
74 (e.g., hydroxyl radical ($\cdot\text{OH}$), O_3), are ubiquitous and play a significant role in the
75 transformation of atmospheric WSOM (Hems et al., 2021; Manfrin et al., 2019).
76 Research conducted by Cai et al. (2020) revealed that the aqueous photochemistry of
77 BB WSOM can produce highly oxygenated compounds, which subsequently enhance
78 the oxidation state of WSOM in atmospheric samples. Furthermore, the $\cdot\text{OH}$
79 photooxidation of BB-derived organic species (e.g., 4-methylsyringol, eugenol) has
80 been found to form light-absorbing products, indicating a potential pathway for
81 secondary organic aerosol (SOA) (Liu et al., 2022; Li et al., 2023; Arciva et al., 2022).
82 Additionally, the $\cdot\text{OH}$ photooxidation of freshly emitted BB WSOM initially result in
83 an increase in its absorption capacity, which is later followed by a photobleaching
84 process during the photoaging (Hems et al., 2021; Wong et al., 2017). These finding



85 underscore the dynamic nature of WSOM due to the photolytic aging, however,
86 further insights into the molecular transformations leading to these observations
87 remain unclear. Moreover, while the chemical composition of WSOM emitted from
88 BB and CC differs, it remains unclear whether distinct classes of molecules exhibit
89 varying behaviors during photochemical processes.

90 To address these inquiries, the photochemical aging of WSOM emitted from both
91 biomass burning and coal combustion was systematically investigated through direct
92 photolysis and OH photooxidation in the aqueous phase. The objectives are (1) to
93 compare the optical evolution of BB and CC WSOM under the photolysis and OH
94 photooxidation; and (2) to elucidate photochemical transformation of BB and CC
95 WSOM at a molecular level by using fourier transform ion cyclotron resonance mass
96 spectrometry (FT-ICR MS). The information obtained will enhance understanding of
97 the atmospheric oxidation processes of combustion-derived WSOM and their
98 subsequent environmental and climatic effects.

99

100 **2. Materials and methods**

101 **2.1. Preparation of WSOM samples**

102 Rice straw (RS) and Yulin coal (YL) were selected as representative biomass and
103 coal fuel materials for the preparation of combustion-derived WSOM samples. These
104 materials are commonly utilized for heating and cooking in rural households,
105 particularly during winter season in northern China. Additionally, RS residue is also
106 burned in agriculture field (Zhang et al., 2023; Huang et al., 2022). The smoke



107 samples emitted from combustion process were collected in a laboratory-controlled
108 combustion system in our laboratory and more detailed information can be seen in our
109 previous studies (Cao et al., 2021; Li et al., 2018). Immediately after collection, the
110 filters were wrapped with baked aluminum foil and stored in a refrigerator (-20°C).

111 Prior to conducting photolysis and photooxidation experiments, the WSOM
112 fraction was extracted using ultrapure-water. Briefly, filter sample was cut into pieces
113 and placed in 100 mL glass bottle, to which 60 mL ultrapure water was added. After
114 ultrasonically extracted for 30 min, the extract was filtered through a $0.22\ \mu\text{m}$
115 polytetrafluoroethylene syringe filter (Anpel, ANPEL Laboratory Technology
116 (Shanghai) Inc.). The organic carbon concentration of WSOM solution was measured
117 before photochemical reaction and diluted to 20 mgC/L by ultrapure water, in
118 accordance with preliminary experimental protocols (Gu et al., 2024; Zhang et al.,
119 2022).

120 **2.2. Photolysis and OH photooxidation experiment**

121 The photolysis and OH photooxidation experiments were conducted in a
122 photoreactor, where quartz cell containing WSOM solution were continuously
123 exposed to radiation. Briefly, 100 mL of 20 mgC/L WSOM solution was magnetically
124 stirred in a 250 mL cylindrical quartz cell equipped with water circulating jacket to
125 maintain a constant temperature of 25°C . For the photolysis experiment, the WSOM
126 solution was irradiated from the top by Xenon lamp (PL-XQ500W, Beijing Princess
127 Technology co. ltd) with an output energy of 500W at 0.2 m. The irradiation energy at
128 the water surface is $12.5\ \text{mW}/\text{cm}^2$ in the range of 290–400 nm. For the $\cdot\text{OH}$



129 photooxidation experiments, 3mM H₂O₂ was added to the WSOM solution as a
130 photolytic source of OH radicals upon irradiation (Zhao et al., 2015; Arciva et al.,
131 2024). For each experiment, 4 mL samples were withdrawn periodically (0, 1, 2, 4, 8,
132 12, 24h) from the reactor and then diluted to 20 mL for further analysis. The
133 photolysis and OH photooxidation experiment were both carry out the dark control
134 synchronously follow the conditions as introduced above. The results showed that no
135 significant changes were observed for the organic carbon content and the UV-vis
136 absorption of WSOM within the reaction time.

137 **2.3. Spectroscopy measurement**

138 The UV-vis absorption of WSOM was measured using a UV-vis
139 spectrophotometer (UV-2600i, Shimadzu, Japan) within the wavelength range of 200
140 – 700 nm. Excitation-emission matrix (EEM) spectra were recorded by
141 three-dimensional fluorescence spectrophotometer (Aqualog, HORIBA Scientific,
142 USA). The scanning ranges for excitation (Ex) and emission (Em) were 240–800 nm
143 and 250–800 nm, respectively. Ultrapure water (18.2MΩcm⁻¹) was used as blank
144 reference and correcting the fluorescence intensity unit by the Raman peak area of
145 water (R.U.). In addition, the corresponding absorption spectra were used to correct
146 the EEM for inner-filter effects (IFE) according to the previous studies if the
147 absorbance was higher than 0.05 at 250 nm (Tang et al., 2020; He and Hur, 2015;
148 Murphy et al., 2013). The PARAFAC modeling procedure was conducted in
149 MATLAB 2021b (Mathwork.Inc, USA) by the drEEM toolkit (Murphy et al., 2018;
150 Pucher et al., 2019). More information and data processing details are provided in



151 Text S1 of Supporting information (SI).

152 **2.4. High-resolution mass spectrometry analysis**

153 The molecular characteristics of WSOM before and after photolysis and OH
154 photooxidation were measured with a solariX XR FT-ICR MS (Bruker Daltonik
155 GmbH, Bremen, Germany) equipped with a 9.4T refrigerated actively shielded
156 superconducting magnet and a Paracell analyzer cell. The WSOM samples used for
157 FT-ICR MS analysis were desalted by solid phase extraction cartridge (Oasis HLB,
158 200 mg, Waters, Milford, MA, USA) as introduced in our previous studies (Song et al.,
159 2019; Song et al., 2018; Song et al., 2022). The detailed measurement condition and
160 the calculation of corresponding indexes (e.g. double bond equivalents (DBE) and
161 modified aromaticity index (AI_{mod})) are described in Text S2 in SI. For better
162 elucidate the transformation of RS and YL WSOM, the photochemical resistant,
163 degraded, and produced molecules were investigated (Fan et al., 2024; Gu et al.,
164 2024).

165

166 **3. Results and discussion**

167 **3.1. Effect of photolysis and ·OH photooxidation on the light absorption of** 168 **WSOM**

169 The absorption spectra of RS and YL WSOM during photolysis and ·OH
170 photooxidation are illustrated in Figure 1a-d. It can be observed that the absorbance of
171 RS WSOM gradually decrease as aging time increasing during both photolysis and
172 ·OH photooxidation, indicating substantial photobleaching (Fan et al., 2024; Zhao et



173 al., 2022). Moreover, the reduction in absorbance during $\cdot\text{OH}$ photooxidation is more
174 obvious than that in photolysis, indicated that RS WSOM undergoes greater
175 degradation during $\cdot\text{OH}$ photooxidation. In contrast, the absorbance of YL WSOM
176 present different variation during the photolysis and $\cdot\text{OH}$ photooxidation. Specifically,
177 the absorbance in the short wavelength range of 210-240 nm decreases gradually with
178 aging time, while the absorbances at wavelengths exceeding 360 nm increase. This
179 phenomenon is characteristic of photoenhancement, which aligns with finding
180 reported in previous studies concerning nitrate-mediated photooxidation of guaiacol
181 and 5-nitroguaiacol as well as photooxidation of mixed aromatic carbonyls (Go et al.,
182 2024; Yang et al., 2021).

183 To quantitatively assess the changes in light-absorbing substances during
184 photolysis and $\cdot\text{OH}$ photooxidation, the absorption coefficients at 254 nm (α_{254}) and
185 365 nm (α_{365}) were calculated (Fan et al., 2024; Zou et al., 2023). As shown in Figure
186 1e, the α_{254} values for both RS and YL WSOM consistently decline during photolysis
187 and $\cdot\text{OH}$ photooxidation, with a more significant reduction observed during $\cdot\text{OH}$
188 photooxidation. These results are consistent with earlier studies on $\cdot\text{OH}$ oxidation and
189 photochemical oxidation of BB WSOM, indicating that the presence of $\cdot\text{OH}$ radicals
190 accelerate the degradation of aromatic structures within WSOM (Fan et al., 2024; Ye
191 et al., 2020). Additionally, the reduction of α_{254} values was always greater for RS
192 WSOM than for YL WSOM, suggesting that RS WSOM are more susceptible to
193 photochemical degradation.

194 The α_{365} values for RS and YL WSOM exhibit different variations under



195 photolysis and $\cdot\text{OH}$ photooxidation. As illustrated in Figure 1f, the α_{365} value for RS
196 WSOM gradually decrease with prolonged photolysis, while it initially increased
197 slightly before decreasing during $\cdot\text{OH}$ photooxidation. Similar observation has been
198 made in the photochemical aging of wood smoke BrC and monomeric phenolic
199 compounds, suggesting the formation of new compounds with significant
200 light-absorbing capacity during the initial stage of $\cdot\text{OH}$ photochemical reaction (Hems
201 et al., 2021; Wong et al., 2017; Lee et al., 2014). In contrast, the α_{365} values of YL
202 WSOM present markedly different trends, increasing during 24h photolysis and
203 initially rising for 12h before decreasing from 12h to 24h during $\cdot\text{OH}$ photooxidation.
204 These results indicates that the products generated from photochemical reaction of YL
205 WSOM possess enhanced light absorbance in the near-UV and visible regions, which
206 are also observed in the aqueous phase oxidation of aromatic compounds such as
207 phenols (Arciva et al., 2024; Smith et al., 2016). The proposed mechanism may
208 involve the aromatization of phenolic compounds and $\cdot\text{OH}$ -functionalization of
209 aromatic compounds, leading to the formation of the strong light-absorbing
210 substances at longer wavelength (Li et al., 2023).

211 **3.2. EEM-PARAFAC of WSOM during the photolysis and $\cdot\text{OH}$ photooxidation**

212 The EEM-PARAFAC model has successfully identified three distinct fluorescent
213 components (C1–C3) within RS and YL WSOM. As shown in Figure 2a, C1 displays
214 excitation/emission peaks at $\text{Ex/Em} = 270/325$ nm, which are attributed to protein-like
215 substances, including tyrosine-like substances (Podgorski et al., 2018; Hu et al., 2023),
216 as well as non-nitrogenous containing species such as phenol-like compounds (Cao et



217 al., 2023). C2 (240, 320/420 nm) and C3 (240/350 nm) both assigned to humic-like
218 substances (Hu et al., 2023; He et al., 2023; Fan et al., 2021). Due to the fluorescence
219 distributed at longer wavelengths are mainly associated of larger molecular weight
220 and highly oxygenated of fluorophores (Cao et al., 2023), thereby suggesting that the
221 longer emission wavelengths of C2 might be associated with highly oxygenated
222 humic-like fluorophores with higher molecular weight and aromaticity, while C3
223 could be more relevant to less oxygenated structures and conjugated systems.
224 Furthermore, fluorophores contain same position with C2 have been observed during
225 the photooxidation of vanillic acid and ozone oxidation of BB BrC (Fan et al., 2021;
226 Tang et al., 2020), indicating C2 may be closely related with the products formed
227 through atmospheric oxidation processes.

228 To quantitatively access the changes in the distribution of fluorophores during the
229 photochemical process, total fluorescence intensity (TFI) was calculated. As depicted
230 in Figure 2d, the TFI values for RS and YL WSOM showed a comparable decline
231 during both photolysis and $\cdot\text{OH}$ photooxidation, with a pronounced reduction during
232 $\cdot\text{OH}$ photooxidation. These results indicate that fluorophores are more susceptible to
233 degradation or quenching by $\cdot\text{OH}$ attacks than by direct photolysis in both BB and CC
234 WSOM. On the one hand, more aromatic structures in WSOM may be disrupted by
235 $\cdot\text{OH}$ radical, resulting a more significant reduction in fluorophores. On the other hand,
236 the $\cdot\text{OH}$ photooxidation also lead to an increase in carboxyl groups, which are the
237 typical electron-withdrawing groups. thereby contributing to a reduction or quenching
238 of fluorescence in WSOM.



Moreover, the relative contribution of the three fluorophores in RS and YL WSOM varied throughout photochemical processes, with more significant changes noted during $\cdot\text{OH}$ photooxidation (Figure 2e-h). It is obvious that the increases in C2 are 49% and 56% for RS and YL WSOM during $\cdot\text{OH}$ photooxidation, which is significantly higher than that 5% and 14% during photolysis. These can be explained by the formation of more highly oxygenated humic-like fluorophores due to $\cdot\text{OH}$ photooxidation (Zhang et al., 2022; Fan et al., 2024). In contrast, fluorophore C3 greatly declined by 35% and 56% for RS and YL WSOM, respectively, during $\cdot\text{OH}$ photooxidation. Previous studies have linked fluorophore C3 to less-oxygenated fluorescent substances resulting from primary combustion (Cao et al., 2023; Chen et al., 2016), which can be oxidated and gradually removed during the $\cdot\text{OH}$ photooxidation process. Comparatively, the contributions of three fluorescent components in RS and YL WSOM both display relatively minor variations under photolysis, suggesting the lower selectivity of photolysis. These notable variations in both the subgroup and intensity of fluorophores suggest their potential utility as indicator of the atmospheric oxidation processes experienced by fresh emissions (Fan et al., 2024; Ye et al., 2025).

3.3. Changes in molecular characteristics of RS and YL WSOM

Figure 3 showed the FT-ICR MS spectra of RS and YL WSOM before and after undergoing photochemical oxidation. A total of 5114 to 6383 molecules were identified within the m/z range of 100-600, with a predominant concentration of peaks observed between 150 to 400. These finding are indicative of the molecular



characteristics typical of organic compounds resulting from BB and coal combustion emissions (Tang et al., 2020; Song et al., 2018; Song et al., 2022). The identified formulae were categorized based on their elemental compositions into four groups: CHO, CHON, CHOS, and CHONS (Tang et al., 2020; Song et al., 2018). As shown in Figure 3, CHO and CHON compounds are the dominant compounds (95.8%-98.4%) in RS WSOM, with minor fluctuations following photolysis and OH photooxidation. These observations align with findings related to BB WSOM subjected to dark OH oxidation and BB smoke aerosols in an oxidation flow reactor (Fan et al., 2024; Zhao et al., 2022). In contrast to RS WSOM, YL WSOM contain not only high content of CHO (47.6%) and CHON (33.1%), but also significant S-containing substances (CHOS and CHONS, 19.2%). Figure 3 reveals notable differences in the composition of compound groups within YL WSOM. The CHO compounds in fresh YL WSOM are 47.6%, which increased to 76.1% and 84.2% after photolysis and OH photooxidation, respectively. Whereas, the CHON compounds decreased from 33.1% to 13.4% and 13.6%, respectively. Additionally, S-containing compounds demonstrated a marked decrease following photolysis and OH photooxidation for YL WSOM. These discrepancies may be attributed to the inherent differences in molecular composition between RS WSOM and YL WSOM, which exhibit varying sensitivities to photolysis and OH photooxidation.

3.3.1. Molecular properties

The intensity weighted average values of various molecular parameters, including molecular weight (MW_w), elemental ratios, double bond equivalents



(DBE_w), modified aromaticity index (AI_{mod, w}) and oxidation state of carbon (OS_{c, w}) of RS and YL WSOM before and after photochemical aging were summarized in Table S1. It is evident that the molecular characteristics of WSOM underwent significant alterations following photolysis and ·OH photooxidation. Specifically, the MW_w value of fresh RS WSOM is 252, which increased to 288 and 319 after photolysis and ·OH photooxidation, respectively. The similar trend was observed for YL WSOM, where the MW_w values increased from 231 to 268 and 303, respectively. These results align with previous studies indicating that the MW values of BB WSOC increased after dark ·OH oxidation and photolysis (Fan et al., 2024; Wong et al., 2019). Such changes may be attributed to the newly formation of higher MW molecules through the oligomerization reactions and the resistance of high MW ones during photochemical aging (Gu et al., 2024; Fan et al., 2024; Go et al., 2024; Waggoner et al., 2015; Carena et al., 2023). Furthermore, it is noteworthy that the MW_w values for both RS and YL WSOM following ·OH photooxidation were greater than that after photolysis, suggesting that ·OH photooxidation exerts a more pronounced aging effect.

As detailed in Table S1, the AI_w value of fresh RS WSOM is 0.44, which subsequently decreased to 0.42 and 0.36 after photolysis and ·OH photooxidation, respectively. Similar variation was noted for YL WSOM, where the AI_w value decreased from 0.56 to 0.52 and 0.47, respectively. Moreover, the reduction in AI_{mod, w} values were more pronounced for both RS and YL WSOM subjected to ·OH photooxidation. These results indicate that the aromatic structures within WSOM



305 were disrupted during photochemical processes, with OH photooxidation resulting in
306 more significant breakdown (Zhao et al., 2022).

307 The O/C_w and $OS_{c,w}$ values were used to estimate the oxidation degree of the
308 formulae in WSOM. As shown in Table S1, the O/C_w of RS WSOM increased from
309 0.38 to 0.43 and 0.59 after photolysis and OH photooxidation, respectively,
310 indicating an increase in the number of O atom within the molecular post-oxidation.
311 Notably, the $OS_{c,w}$ values exhibited a similar trend to that of O/C_w . These observations
312 are consistent with findings related to BB WSOC under dark oxidation and the
313 photochemical transformation of DOM (Gu et al., 2024; Zhang et al., 2022; Fan et al.,
314 2024), suggesting a substantial incorporation of O-containing functional groups into
315 carbon structures during the photolysis and OH oxidation. The O/C_w and $OS_{c,w}$
316 values for YL WSOM demonstrated analogous changes following OH
317 photooxidation, increasing from 0.46 to 0.57 and from -0.11 to 0.11, respectively.
318 However, the O/C_w and $OS_{c,w}$ values for YL WSOM exhibit slight decrease after
319 photolysis, declining from 0.46 to 0.43 and from -0.11 to -0.15, respectively. These
320 findings indicate that the photochemical evolution of WSOM is significantly
321 influenced by their molecular composition. Nonetheless, it is undoubtedly that the
322 O/C_w and $OS_{c,w}$ values of aged WSOM resulting from OH photooxidation are
323 significantly higher than those resulting from photolysis, indicating a more robust
324 oxidation process.

325 To further elucidate the molecular distribution of WSOM, van Krevelen (VK)
326 diagrams were constructed by plotting the H/C ratio versus O/C ratio. As indicated in



327 Figure S1, the identified compounds were classified into seven distinct regions (Sun et
328 al., 2023; Song et al., 2018): (I) lipids-like, (II) protein/animal sugars, (III)
329 carbohydrates-like, (IV) unsaturated hydrocarbons, (V) lignin/CRAMs-like, (VI)
330 condensed aromatic, and (VII) tannins. It is obvious that lignin/CRAMs-like
331 compounds emerged as the predominant constituents, comprising 83.1% and 88.4% of
332 the fresh RS and YL WSOM (Table S2), respectively. The proportion of these
333 compounds remained stable following photolysis; however, a decline was observed
334 following OH photooxidation, with the contents decreasing from 83.1% to 63.3% for
335 RS WSOM and from 88.4% to 73.9% for YL WSOM. Lipid compounds were also
336 identified in both fresh RS and YL WSOM, with relative higher contents in RS
337 WSOM, however, a significant reduction in lipid content was noted after OH
338 photooxidation for both RS WSOM and YL WSOM. This trend aligns with
339 observations of DOM under UV irradiation, where lignin and lipids were identified as
340 the most active component involved in molecular conversion (Gu et al., 2024).
341 Conversely, the content of tannins-like substances in both RS and YL WSOM greatly
342 increased due to OH photooxidation. This suggests that the attack by OH radical leads
343 to the formation of more polar tannins compounds, indicating the potential
344 contribution of multiple oxygen-enrich groups (i.e., carboxyl) to the aged WSOM.
345 Such additional functional groups may enhance the polarity and reactivity of WSOM,
346 thereby influencing their optical properties, chemical reactivity, and interactions with
347 other atmospheric components. It is noteworthy that more condensed aromatic
348 compounds were observed in aged WSOM subjected to photochemical process,



349 especially OH photooxidation (e.g., the left and bottom of VK diagrams, Figure S1).
350 Furthermore, as shown in Table S2, the content of condensated aromatic compounds
351 increased from 1.08% to 1.55% and 4.86% (RS WSOM) and 2.86% to 4.08% and
352 5.38% (YL WSOM) after photolysis and OH photooxidation, respectively. These
353 findings strongly support the notion that condensated aromatic molecules are formed
354 through the photochemical reactions, particularly the OH photooxidation reaction.

355 **3.3.2. Comparison of the transformation of WSOM induced by photolysis** 356 **and OH photooxidation**

357 To enhance the understanding of molecular transformations occurring in RS and
358 YL WSOM, the photochemical resistant, degraded, and produced molecules were
359 investigated. The formulae identified both before and after photochemical aging were
360 assigned to resistant; unique formulae before reaction represented the degraded
361 molecules; whereas unique formulae after reaction were considered to newly
362 produced molecules (Figure 4) (Gu et al., 2024; Fan et al., 2024; Zhao et al., 2022). It
363 is important to acknowledge that the molecules categorized as resistant may also
364 include those generated from the photochemical reaction, but with the formulae to
365 those in fresh molecules. As presented in Table S3, approximately 14.9% of the total
366 number of formulas in fresh RS WSOM and 23.1% in YL WSOM were degraded
367 through photolysis, resulting in the formation of 26.0% (RS WSOM) and 31.7 % (YL
368 WSOM) of newly produced formulae in the aged WSOM, respectively. In contrast,
369 much higher content of formulae (61.6% of RS WSOM and 65.0% of YL WSOM)
370 were degraded by OH photooxidation and led to higher content (57.0%-61.0%) of



371 new formulae. These findings suggest that OH photooxidation possesses greater
372 oxidative potential, resulting in a more substantial degradation and transformation of
373 molecules.

374 As shown in Figure 4, the majorities of the degraded molecules were found in
375 regions characterized by in O/C (<0.6) within VK diagram. In contrast, the newly
376 produced molecules were concentrated in the regions of $0.3 < \text{O/C} < 0.9$. This finding
377 implies that molecules with low O/C underwent oxidation during photolysis and OH
378 photooxidation processes, resulting in their transformation into oxygen-enriched
379 structures, especially through OH photooxidation. Furthermore, notable differences
380 were observed in the VK diagrams corresponding to photolysis and OH
381 photooxidation. It is obvious that the degraded molecules from RS and YL WSOM
382 were distributed in the same region of the VK diagrams; however, the newly formed
383 molecules resulting from distinct photochemical reactions were distributed across
384 different regions (Figure S2). For example, the molecules produced from the
385 photolysis of RS WSOM primarily located in the range of $0.3 < \text{O/C} < 0.7$ and $0.5 <$
386 $\text{H/C} < 1.7$, whereas those generated through OH photooxidation were found in two
387 separate regions. The majorities of these molecules were concentrated in the range 0.4
388 $< \text{O/C} < 0.9$ and $0.4 < \text{H/C} < 2.0$, indicating a higher formation of oxygenated
389 compounds through OH photooxidation. As illustrated in Figure 4, the presence of
390 tannin-like compounds in the molecules produced after OH photooxidation were
391 much higher than that formed after photolysis for both RS and YL WSOM. These
392 results indicate that the OH photooxidation process substantially enhanced the



393 abundance of O-containing functional groups within the molecules, as well as the
394 overall oxidation state of WSOM. Additionally, certain condensed aromatic
395 molecules were identified in the regions VI in Figure 4 and S2, showing the newly
396 production of condensed aromatics during OH photooxidation. According to Table
397 S4, these newly formed condensed molecules were identified in both RS and YL
398 WSOM, accounting for 11.6% and 4.7% of the total produced molecules (intensity
399 weighted). These compounds exhibited lower H/C_w (0.55 and 0.60) and O/C_w (0.14
400 and 0.17) ratios alongside higher $AI_{mod,w}$ (0.76 and 0.77) values, indicating a
401 predominance of highly aromatic structures. Moreover, they consisted with CHO,
402 CHON, CHOS, and CHONS, among which CHON is the highest components (57.7%
403 and 58.0%) for both RS and YL WSOM. It is noteworthy the O/N_w ratios for CHON
404 and the O/S_w ratios for CHOS were relatively low, suggesting that the N-containing
405 and S-containing functional group here may mainly comprised with reduced groups.
406 According to previous studies, the condensed aromatic compounds are usually
407 assigned to combustion derived BC molecules, i.e., dissolved black carbon. However,
408 our study suggesting the OH photochemical oxidation may also lead to the formation
409 of BC-like molecules.

410 As shown in Table S5, the degraded molecules exhibited lower $AI_{mod,w}$ values
411 and O/C_w ratio, and higher MW_w , DBE_w , and H/C_w values compared to the resistant
412 molecules. For example, the $AI_{mod,w}$ value and O/C_w ratio of the degraded molecules
413 of RS WSOM are 0.33 and 0.33, respectively, which are lower than the corresponding
414 values of 0.38 and 0.45 for the resistant molecules during photolysis. Conversely, the



415 MW_w , DBE_w , and H/C_w ratio for the degraded molecules are 392, 8.3, and 1.29,
416 significantly higher than that for the resistant molecules. Similar differences were
417 noted between the resistant and degraded molecules in RS WSOM subjected to OH
418 photooxidation, as well as in YL WSOM underwent both photolysis and OH
419 photooxidation. These differences indicate that the WSOM susceptible to
420 photochemical aging are those molecules with higher molecular weight, double bond
421 intensity, and aliphatic structures but with lower aromaticity and O-containing group.

422 In comparison, the newly formed molecules within RS and YL WSOM
423 demonstrate elevated O/C_w , DBE_w , and MW_w values. For example, the newly formed
424 molecules for RS WSOM resulting from photolysis possess higher O/C_w (0.48),
425 DBE_w (12.0), and MW_w (473) than the degraded molecules. These results indicate that
426 photolysis generates a greater quantity of high molecular weight compounds, which
427 also contain more oxygenated functional groups, such carbonyl. Furthermore, the
428 differences between the degraded and resistant molecules during OH photooxidation
429 are pronounced than that during the photolysis process, suggesting that a more
430 extensive aging reaction occurs during OH photooxidation. However, the variation in
431 $AI_{mod,w}$ value between the degraded and produced molecules differ across samples. In
432 the case of RS WSOM, the produced molecules exhibit higher $AI_{mod,w}$ values than the
433 degraded molecules during photolysis process, yet they are very similar during OH
434 photooxidation. Additionally, distinct changes in $AI_{mod,w}$ values were observed for YL
435 WSOM during photolysis, where the $AI_{mod,w}$ value of newly produced molecules is
436 lower than that of degraded molecules, and the proportion of aromatic and condensed



437 aromatic compounds decreased for YL WSOM after photolysis. These discrepancies
438 may be due to the produced molecules defined represent only a subset of those
439 generated during the aging process.

440 **3.4. Comparison of the photochemical evolution of WSOM from biomass** 441 **burning and coal combustion**

442 The photochemical evolution of WSOM originating from BB and CC were
443 comparably investigated in our study. Our results indicate that the absorption spectra
444 of RS and YL WSOM exhibit a decreasing trend at ranges below 240 nm during
445 photolysis and OH photooxidation. However, notable differences were observed
446 between the two types of WSOM. For example, the α_{365} value for RS WSOM
447 consistently decreased throughout the photolysis and OH photooxidation, whereas
448 YL WSOM displayed a progressive increase in this value. These differences may be
449 attributed to the inherent differences in WSOM derived from biomass burning
450 compared to that from coal combustion (Cao et al., 2021; Song et al., 2018). The
451 results indicate that WSOM derived from various sources may undergo distinct
452 changes in absorbance during photochemical aging, potentially leading to varying
453 impacts on climate change and radiation balance.

454 Furthermore, the TFI values for both RS and YL WSOM exhibit a gradual
455 decline during photolysis and OH photooxidation with no significant differences
456 between the two. However, the variations in fluorophore composition within RS and
457 YL WSOM were markedly different. For example, three fluorophores in RS WSOM
458 remained relative stable during photolysis, while the less-oxygenated fluorophores C3



459 in YL WSOM gradually decreased. These may indicate that the fluorophores C3 in
460 YL WSOM are more susceptible to photolytic degradation. These results suggest that
461 the molecular composition of identical fluorescent component in WSOM derived
462 from different sources may exhibit notable differences.

463 As previously discussed, there are notable similarities in the molecular
464 alterations observed in RS and YL WSOM after photolysis aging. Specifically, the
465 MW_w values for both RS and YL WSOM exhibited an increase after photochemical
466 processes, suggesting the formation of high MW molecules through the
467 oligomerization reaction and the resistance of high MW ones during photochemical
468 aging. Furthermore, the $AI_{mod,w}$ values always decreased, while the O/C ratios
469 consistently increased for the both aged RS and YL WSOM. These results indicate the
470 broken of aromatic structures and the formation of O-containing groups within
471 WSOM as a result of photochemical processes. However, distinct differences in
472 molecular characteristics between RS and YL WSOM were observed, which may
473 influence their respective changes due to photochemical reactions. For example,
474 CHON compound in RS WSOM exhibit minor variation after photochemical
475 reactions, whereas it greatly decreased in YL WSOM. Notably, RS WSOM
476 experienced a greater degradation of lipids during photolysis and OH photooxidation,
477 leading to the production of carbohydrate or tannin-like substances (Table S2).

478

479 **4. Environmental significance**

480 Biomass and coal combustion releases considerable quantities of WSOM into the



481 atmosphere, which undergo significant photochemical transformations under light
482 irradiation, resulting in considerable uncertainty regarding its physical and chemical
483 characteristics, as well as reactivity in the atmospheric environment. The present
484 study investigated the optical and molecular evolution in WSOM derived from BB
485 and CC (i.e., RS and YL WSOM) during aqueous phase photolysis and OH
486 photooxidation. The findings indicate a marked reduction in light absorption of RS
487 WSOM at 365 nm during photochemical processes and more pronounced for the OH
488 photooxidation, indicating a stronger photobleaching. In contrast, a notable
489 photoenhancement was observed for YL WSOM during the photochemical processes.
490 These results suggest that the alteration in light absorption of WSOM are closely
491 linked to the chemical composition of fresh WSOM.

492 At the molecular level, the degradation of aromatic structures within WSOM was
493 evident, accompanied by the formations of O-containing polar groups (e.g., carbonyl,
494 carboxyl groups), as a result of the photochemical reactions, particularly during OH
495 photooxidation. These results indicate that the oxidation degree and severity of OH
496 photooxidation is much higher than that of photolysis, leading to the variations in the
497 optical properties of WSOM. It is worth noting that the polymerization occurs in
498 both photolysis and OH photooxidation, especially in OH photooxidation, as
499 evidenced by an increase in MW_w and the formation of condensed aromatic
500 compounds. These condensed aromatic compounds exhibit similarities to the
501 chemical and molecular structures of combustion derived BC molecules.
502 Therefore, OH photochemical oxidation may be a potential formation mechanism of



503 BC-like materials.

504 It is important to note that this study focused solely on WSOM produced from a
505 specific type of biomass and coal samples in laboratory simulated system, which may
506 nor accurately reflect the complexities of combustion processes in real-world
507 scenarios. Therefore, a more comprehensive investigation into the photochemical
508 aging of WSOM from diverse biomass and coal sources, as well as under various
509 conditions in natural environments, is warranted. Furthermore, it is clear that the
510 photochemical aging processes significantly influences their environmental, climate,
511 and health effects, necessitating further exploration in future research endeavors.

512

513 **Data availability.** The research data can used in this study are available from
514 Jianzhong Song (songjzh@gig.ac.cn).

515

516 **Author contributions.** T. Cao and J. Song designed the research and wrote the paper.
517 T. Cao, C. Xu, H. Chen and H. Song, analyzed the combustion-derived WSOM
518 samples during photochemical process. B. Jiang analyzed the WSOM samples by
519 FT-ICR MS. J. Li, Y. Zhong, and P. Peng commented and revised the paper.

520

521 **Competing interests.** The authors declare that they have no conflict of interest

522

523 **Acknowledgments.** This study was supported by the National Natural Science
524 Foundation of China (42192514), Guangdong Major Project of Basic and Applied



525 Basic Research (2023B0303000007), and the Guangdong Foundation for Program of
526 Science and Technology Research (2023B1212060049).

527

528 **References**

529 Arciva, S., Ma, L., Mavis, C., Guzman, C., Anastasio, C. Formation and loss of light
530 absorbance by phenolic aqueous SOA by OH and an organic triplet excited state.
531 Atmos. Chem. Phys., 24, 4473-4485, <https://doi.org/10.5194/acp-24-4473-2024>,
532 2024.

533 Arciva, S., Niedek, C., Mavis, C., Yoon, M., Sanchez, M. E., Zhang, Q., Anastasio, C.
534 Aqueous OH Oxidation of Highly Substituted Phenols as a Source of Secondary
535 Organic Aerosol. Environ. Sci. Technol., 56, 9959-9967,
536 <https://doi.org/10.1021/acs.est.2c02225>, 2022.

537 Bali, K., Banerji, S., Campbell, J. R., Bhakta, A. V., Chen, L. W. A., Holmes, C. D.,
538 Mao, J. Measurements of brown carbon and its optical properties from boreal
539 forest fires in Alaska summer. Atmos. Environ., 324, 120436,
540 <https://doi.org/10.1016/j.atmosenv.2024.120436>, 2024.

541 Bates, J. T., Fang, T., Verma, V., Zeng, L., Weber, R. J., Tolbert, P. E., Abrams, J. Y.,
542 Sarnat, S. E., Klein, M., Mulholland, J. A., Russell, A. G. Review of Acellular
543 Assays of Ambient Particulate Matter Oxidative Potential: Methods and
544 Relationships with Composition, Sources, and Health Effects. Environ. Sci.
545 Technol., 53, 4003-4019, <https://doi.org/10.1021/acs.est.8b03430>, 2019.

546 Bhattu, D., Tripathi, S. N., Bhowmik, H. S., Moschos, V., Lee, C. P., Rauber, M.,



547 Salazar, G., Abbaszade, G., Cui, T., Slowik, J. G., Vats,, P., Mishra, S.,
548 Lalchandani, V., Satish, R., Rai, P., Casotto, R., Tobler, A., Kumar, V., Hao, Y.,
549 Qi, L., Khare, P., Manousakas, M., Wang, Q., Han, Y., Tian, J., Darfeuil, S.,
550 Minguillon, M., Hueglin, C., Conil, S., Rastogi, N., Srivastava, A., Ganguly, D.,
551 Bjelic, S., Canonaco, F., Schnelle-Kreis, J., Dominutti, P. A., Jaffrezo, J., Szidat,
552 S., Chen, Y., Cao, J., Baltensperger, U., Uzu, G., Daellenbach, K. R., Haddad, I.,
553 Prévôt, A. S. H. Local incomplete combustion emissions define the PM_{2.5}
554 oxidative potential in Northern India. Nat. Commun., 15, 3517,
555 <https://doi.org/10.1038/s41467-024-47785-5>, 2024.

556 Bikkina, P., Sarma, V. V. S. S., Kawamura, K., Bikkina, S., Kunwar, B., Sherin, C. K.
557 Chemical characterization of wintertime aerosols over the Arabian Sea: Impact
558 of marine sources and long-range transport. Atmos. Environ., 239, 117749,
559 <https://doi.org/10.1016/j.atmosenv.2020.117749>, 2020.

560 Cai, J., Zeng, X., Zhi, G., Gligorovski, S., Sheng, G., Yu, Z., Wang, X., Peng, P.
561 Molecular composition and photochemical evolution of water-soluble organic
562 carbon (WSOC) extracted from field biomass burning aerosols using
563 high-resolution mass spectrometry. Atmos. Chem. Phys., 20, 6115-6128,
564 <https://doi.org/10.5194/acp-20-6115-2020>, 2020.

565 Cao, T., Li, M., Xu, C., Song, J., Fan, X., Li, J., Jia, W., Peng, P. Technical note:
566 Chemical composition and source identification of fluorescent components in
567 atmospheric water-soluble brown carbon by excitation–emission matrix
568 spectroscopy with parallel factor analysis – potential limitations and applications.



- 569 Atmos. Chem. Phys., 23, 2613-2625, <https://doi.org/10.5194/acp-23-2613-2023>,
570 2023.
- 571 Cao, T., Li, M., Zou, C., Fan, X., Song, J., Jia, W., Yu, C., Yu, Z., Ping, P. Chemical
572 composition, optical properties, and oxidative potential of water- and
573 methanol-soluble organic compounds emitted from the combustion of biomass
574 materials and coal. Atmos. Chem. Phys., 21, 13187-13205,
575 <https://doi.org/10.5194/acp-21-13187-2021>, 2021.
- 576 Carena, L., Zoppi, B., Sordello, F., Fabbri, D., Minella, M., Minero, C.
577 Phototransformation of Vanillin in Artificial Snow by Direct Photolysis and
578 Mediated by Nitrite. Environ. Sci. Technol., 57, 8785-8795,
579 <https://doi.org/10.1021/acs.est.3c01931>, 2023.
- 580 Casotto, R., Skiba, A., Rauber, M., Strahl, J., Tobler, A., Bhattu, D., Lamkaddam, H.,
581 Manousakas, M. I., Salazar, G., Cui, T., Canonaco, F., Samek, L., Ryś, A.,
582 Haddad, I. E., Kasper-Giebl, A., Baltensperger, U., Necki, J., Szidat, S., Styszko,
583 K., Slowik, J. G., Prévôt, A. S.H., Daellenbach, K. R. Organic aerosol sources in
584 Krakow, Poland, before implementation of a solid fuel residential heating ban.
585 Sci. Total. Environ., 855, 158655,
586 <https://doi.org/10.1016/j.scitotenv.2022.158655>, 2023.
- 587 Ceamanos, X., Coopman, Q., George, M., Riedi, J., Parrington, M., Clerbaux, C.
588 Remote sensing and model analysis of biomass burning smoke transported across
589 the Atlantic during the 2020 Western US wildfire season. Sci. Rep., 13, 16014,
590 <https://doi.org/10.1038/s41598-023-39312-1>, 2023.



- 591 Chen, Q., Wang, M., Wang, Y., Zhang, L., Li, Y., Han, Y. Oxidative Potential of
592 Water-Soluble Matter Associated with Chromophoric Substances in PM_{2.5} over
593 Xi'an, China. *Environ. Sci. Technol.*, 53, 8574-8584,
594 <https://doi.org/10.1021/acs.est.9b01976>, 2019.
- 595 Chen, Q., Miyazaki, Y., Kawamura, K., Matsumoto, K., Coburn, S., Volkamer, R.,
596 Iwamoto, Y., Kagami, S., Deng, Y., Ogawa, S., Ramasamy, S., Kato, S., Ida, S.,
597 Kajii, Y., Mochida, M. Characterization of Chromophoric Water-Soluble Organic
598 Matter in Urban, Forest, and Marine Aerosols by HR-ToF-AMS Analysis and
599 Excitation-Emission Matrix Spectroscopy. *Environ. Sci. Technol.*, 50,
600 10351-10360, <https://doi.org/10.1021/acs.est.6b01643>, 2016.
- 601 Choudhary, V., Gupta, T., Zhao, R. Evolution of Brown Carbon Aerosols during
602 Atmospheric Long-Range Transport in the South Asian Outflow and Himalayan
603 Cryosphere. *ACS Earth. Space. Chem.*, 6, 2335-2347,
604 <https://doi.org/10.1021/acsearthspacechem.2c00047>, 2022.
- 605 Dasari, S., Andersson, A., Bikkina, S., Holmstrand, H., Budhavant, K., Satheesh, S.,
606 Asmi, E., Kesti, J., Backman, J., Salam, A., Bisht, D. S., Tiwari, S., Hameed,
607 Z., Gustafsson, Ö. Photochemical degradation affects the light absorption of
608 water-soluble brown carbon in the South Asian outflow. *Sci. Adv.*, 5, eaau8066,
609 <https://doi.org/10.1126/sciadv.aau8066>, 2019.
- 610 Fan, X., Xie, S., Yu, X., Cheng, A., Chen, D., Ji, W., Liu, X., Song, J., Peng, P.
611 Molecular-level transformations of biomass burning-derived water-soluble
612 organic carbon during dark aqueous OH oxidation: Insights from absorption,



613 fluorescence, high-performance size exclusion chromatography and
614 high-resolution mass spectrometry analysis. *Sci. Total. Environ.*, 912, 169290,
615 <https://doi.org/10.1016/j.scitotenv.2023.169290>, 2024.

616 Fan, X., Cai, F., Xu, C., Yu, X., Wang, Y., Xiao, X., Ji, W., Cao, T., Song, J., Peng, P.
617 Molecular weight-dependent abundance, absorption, and fluorescence
618 characteristics of water-soluble organic matter in atmospheric aerosols. *Atmos.*
619 *Environ.*, 247, 118159, <https://doi.org/10.1016/j.atmosenv.2020.118159>, 2021.

620 Gallo, F., Uin, J., Sanchez, K. J., Moore, R. H., Wang, J., Wood, R., Mei, F., Flynn, C.,
621 Springston, S., Azevedo, E. B., Kuang, C. A., Aiken, A. C. Long-range
622 transported continental aerosol in the eastern North Atlantic: three multiday
623 event regimes influence cloud condensation nuclei. *Atmos. Chem. Phys.*, 23,
624 4221-4246, <https://doi.org/10.5194/acp-23-4221-2023>, 2023.

625 Go, B. R., Li, Y. J., Huang, D. D., Chan, C. K. Aqueous-Phase Photoreactions of
626 Mixed Aromatic Carbonyl Photosensitizers Yield More Oxygenated, Oxidized,
627 and less Light-Absorbing Secondary Organic Aerosol (SOA) than Single
628 Systems. *Environ. Sci. Technol.*, 58, 7924-7936,
629 <https://doi.org/10.1021/acs.est.3c10199>, 2024.

630 Gu, X., Chen, B., Liu, H., Feng, Y., Wang, B., He, S., Feng, M., Pan, G., Han, S.
631 Photochemical behavior of dissolved organic matter derived from Alternanthera
632 philoxeroides hydrochar: Insights from molecular transformation and
633 photochemically reactive intermediates. *J. Hazard. Mater.*, 461, 132591,
634 <https://doi.org/10.1016/j.jhazmat.2023.132591>, 2024.



- 635 He, T., Wu, Y., Wang, D., Cai, J., Song, J., Yu, Z., Zeng, X., Peng, P. Molecular
636 compositions and optical properties of water-soluble brown carbon during the
637 autumn and winter in Guangzhou, China. *Atmos. Environ.*, 296, 119573,
638 <https://doi.org/10.1016/j.atmosenv.2022.119573>, 2023.
- 639 He, W., Hur, J. Conservative behavior of fluorescence EEM-PARAFAC components
640 in resin fractionation processes and its applicability for characterizing dissolved
641 organic matter. *Water. Res.*, 83, 217-226,
642 <https://doi.org/10.1016/j.watres.2015.06.044>, 2015.
- 643 Hems, R. F., Schnitzler, E. G., Liu-Kang, C., Cappa, C. D., Abbatt, J. P. D. Aging of
644 Atmospheric Brown Carbon Aerosol. *ACS Earth. Space. Chem.*, 5, 722-748,
645 <https://doi.org/10.1021/acsearthspacechem.0c00346>, 2021.
- 646 Hu, T., Luo, M., Qi, Y., He, D., Chen, L., Xu, Y., Chen, D. Molecular evidence for the
647 production of labile, sulfur-bearing dissolved organic matter in the seep
648 sediments of the South China Sea. *Water. Res.*, 233, 119732,
649 <https://doi.org/10.1016/j.watres.2023.119732>, 2023.
- 650 Huang, S., Luo, Y., Wang, X., Zhang, T., Lei, Y., Zeng, Y., Sun, J., Che, H., Xu, H.,
651 Cao, J., Shen, Z. Optical properties, chemical functional group, and oxidative
652 activity of different polarity levels of water-soluble organic matter in PM_{2.5}
653 from biomass and coal combustion in rural areas in Northwest China. *Atmos.*
654 *Environ.*, 283, 119179, <https://doi.org/10.1016/j.atmosenv.2022.119179>, 2022.
- 655 Jiang, H., Cai, J., Feng, X., Chen, Y., Wang, L., Jiang, B., Liao, Y., Li, J., Zhang, G.,
656 Mu, Y., Chen, J. Aqueous-Phase Reactions of Anthropogenic Emissions Lead to



657 the High Chemodiversity of Atmospheric Nitrogen-Containing Compounds
658 during the Haze Event. *Environ. Sci. Technol.*, 57, 16500-16511,
659 <https://doi.org/10.1021/acs.est.3c06648>, 2023.

660 Lee, H. J., Aiona, P. K., Laskin, A., Laskin, J., Nizkorodov, S. A. Effect of solar
661 radiation on the optical properties and molecular composition of laboratory
662 proxies of atmospheric brown carbon. *Environ. Sci. Technol.*, 48, 10217-10226,
663 <https://doi.org/10.1021/es502515r>, 2014.

664 Lee, W. C., Deng, Y., Zhou, R., Itoh, M., Mochida, M., Kuwata, M. Water Solubility
665 Distribution of Organic Matter Accounts for the Discrepancy in Hygroscopicity
666 among Sub- and Supersaturated Humidity Regimes. *Environ. Sci. Technol.*, 56,
667 17924-17935, <https://doi.org/10.1021/acs.est.2c04647>, 2022.

668 Li, F., Tang, S., Lv, J., He, A., Wang, Y., Liu, S., Cao, H., Zhao, L., Wang, Y., Jiang, G.
669 Molecular-Scale Investigation on the Formation of Brown Carbon Aerosol via
670 Iron-Phenolic Compound Reactions in the Dark. *Environ. Sci. Technol.*, 57,
671 11173-11184, <https://doi.org/10.1021/acs.est.3c04263>, 2023.

672 Li, M., Fan, X., Zhu, M., Zou, C., Song, J., Wei, S., Jia, W., Peng, P. Abundances and
673 light absorption properties of brown carbon emitted from residential coal
674 combustion in China. *Environ. Sci. Technol.*, 53, 595-603,
675 <https://doi.org/10.1021/acs.est.8b05630>, 2018.

676 Liu, C., Chen, D., Chen, X. Atmospheric Reactivity of Methoxyphenols: A Review.
677 *Environ. Sci. Technol.*, 56, 2897-2916, <https://doi.org/10.1021/acs.est.1c06535>,
678 2022.



679 Liu, J., Chang, M., Cheng, Z., Zhu, S., Ding, P., Liu, F., Li, J., Zhang, G. High
680 Contribution of South Asian Biomass Burning to Southeastern Tibetan Plateau
681 Air: New Evidence from Radiocarbon Measurement. *Environ. Sci. Technol. Lett.*,
682 8, 1026-1031, <https://doi.org/10.1021/acs.estlett.1c00860>, 2021.

683 Malavelle, F. F., Haywood, J. M., Mercado, L. M., Folberth, G. A., Bellouin, N., Sitch,
684 S., Artaxo, P. Studying the impact of biomass burning aerosol radiative and
685 climate effects on the Amazon rainforest productivity with an Earth system
686 model. *Atmos. Chem. Phys.*, 19, 1301-1326,
687 <https://doi.org/10.5194/acp-19-1301-2019>, 2019.

688 Manfrin, A., Nizkorodov, S. A., Malecha, K. T., Getzinger, G. J., McNeill, K.,
689 Borduas-Dedekind, N. Reactive Oxygen Species Production from Secondary
690 Organic Aerosols: The Importance of Singlet Oxygen. *Environ. Sci. Technol.*, 53,
691 8553-8562, <https://doi.org/10.1021/acs.est.9b01609>, 2019.

692 Murphy, K. R., Stedmon, C. A., Graeber, D., Bro, R. Fluorescence spectroscopy and
693 multi-way techniques. *PARAFAC. Anal. Meth.*, 5, 6557,
694 <https://doi.org/10.1039/c3ay41160e>, 2013.

695 Murphy, K. R., Timko, S. A., Gonsior, M., Powers, L. C., Wunsch, U. J., Stedmon, C.
696 A. Photochemistry Illuminates Ubiquitous Organic Matter Fluorescence Spectra.
697 *Environ. Sci. Technol.*, 52, 11243-11250, <https://doi.org/10.1021/acs.est.8b02648>,
698 2018.

699 Podgorski, D. C., Zito, P., McGuire, J. T., Martinovic-Weigelt, D., Cozzarelli, I. M.,
700 Bekins, B. A., Spencer, R. G. M. Examining Natural Attenuation and Acute



701 Toxicity of Petroleum-Derived Dissolved Organic Matter with Optical
702 Spectroscopy. Environ. Sci. Technol., 52, 6157-6166,
703 <https://doi.org/10.1021/acs.est.8b00016>, 2018.

704 Pucher, M., Wünsch, U., Weigelhofer, G., Murphy, K., Hein, T., Graeber, D. staRdom:
705 Versatile Software for Analyzing Spectroscopic Data of Dissolved Organic
706 Matter in R. Water., 11, 11, <https://doi.org/10.3390/w11112366>, 2019.

707 Schnitzler, E. G., Gerrebos, N. G. A., Carter, T. S., Huang, Y., Heald, C. L., Bertram,
708 A. K., Abbatt, J. P. D. Rate of atmospheric brown carbon whitening governed by
709 environmental conditions. P. Natl. Acad. Sci. USA, 119, e2205610119,
710 <https://doi.org/10.1073/pnas.2205610119>, 2022.

711 Smith, J. D., Kinney, H., Anastasio, C. Phenolic carbonyls undergo rapid aqueous
712 photodegradation to form low-volatility, light-absorbing products. Atmos.
713 Environ., 126, 36-44, <https://doi.org/10.1016/j.atmosenv.2015.11.035>, 2016.

714 Song, J., Li, M., Jiang, B., Wei, S., Fan, X., Peng, P. Molecular Characterization of
715 Water-Soluble Humic like Substances in Smoke Particles Emitted from
716 Combustion of Biomass Materials and Coal Using Ultrahigh-Resolution
717 Electrospray Ionization Fourier Transform Ion Cyclotron Resonance Mass
718 Spectrometry. Environ. Sci. Technol., 52, 2575-2585,
719 <https://doi.org/10.1021/acs.est.7b06126>, 2018.

720 Song, J., Li, M., Zou, C., Cao, T., Fan, X., Jiang, B., Yu, Z., Jia, W., Peng, P.
721 Molecular Characterization of Nitrogen-Containing Compounds in Humic-like
722 Substances Emitted from Biomass Burning and Coal Combustion. Environ. Sci.



- Technol., 56, 119-130, <https://doi.org/10.1021/acs.est.1c04451>, 2022.
- Song, J., Li, M., Fan, X., Zou, C., Zhu, M., Jiang, B., Yu, Z., Jia, W., Liao, Y., Peng, P.
- Molecular Characterization of Water- and Methanol-Soluble Organic
- Compounds Emitted from Residential Coal Combustion Using
- Ultrahigh-Resolution Electrospray Ionization Fourier Transform Ion Cyclotron
- Resonance Mass Spectrometry. Environ. Sci. Technol., 53, 13607-13617,
- <https://doi.org/10.1021/acs.est.9b04331>, 2019.
- Sumlin, B. J., Pandey, A., Walker, M. J., Pattison, R. S., Williams, B. J., Chakrabarty,
- R. K. Atmospheric Photooxidation Diminishes Light Absorption by Primary
- Brown Carbon Aerosol from Biomass Burning. Environ. Sci. Technol. Lett., 4,
- 540-545, <https://doi.org/10.1021/acs.estlett.7b00393>, 2017.
- Sun, W., Guo, Z., Peng, X., Lin, J., Fu, Y., Yang, Y., Zhang, G., Jiang, B., Liao, Y.,
- Chen, D., Wang, X., Bi, X. Molecular characteristics, sources and transformation
- of water-insoluble organic matter in cloud water. Environ. Pollut., 325, 121430,
- <https://doi.org/10.1016/j.envpol.2023.121430>, 2023.
- Sun, Y., Zhang, Q., Zheng, M., Ding, X., Edgerton, E. S., Wang, X. Characterization
- and source apportionment of water-soluble organic matter in atmospheric fine
- particles (PM_{2.5}) with high-resolution aerosol mass spectrometry and GC-MS.
- Environ. Sci. Technol., 45, 4854-4861, <https://doi.org/10.1021/es200162h>, 2011.
- Tang, J., Li, J., Su, T., Han, Y., Mo, Y., Jiang, H., Cui, M., Jiang, B., Chen, Y., Tang, J.,
- Song, J., Peng, P., Zhang, G. Molecular compositions and optical properties of
- dissolved brown carbon in biomass burning, coal combustion, and vehicle



745 emission aerosols illuminated by excitation–emission matrix spectroscopy and
746 Fourier transform ion cyclotron resonance mass spectrometry analysis. *Atmos.*
747 *Chem. Phys.*, 20, 2513–2532, <https://doi.org/10.5194/acp-20-2513-2020>, 2020.

748 Waggoner, D. C., Chen, H. M., Willoughby, A. S., Hatcher, P. G. Formation of black
749 carbon-like and alicyclic aliphatic compounds by hydroxyl radical initiated
750 degradation of lignin. *Organ. Geochem.*, 82, 69–76,
751 <https://doi.org/10.1016/j.orggeochem.2015.02.007>, 2015.

752 Wang, L., Shen, Z., Lu, D., Zhang, Q., Zhang, T., Lei, Y., Xu, H. Water-soluble
753 components in rainwater over Xi'an in northwest China: Source apportionment
754 and pollution controls effectiveness evaluation. *Atmos. Pollut. Res.*, 10, 395–403,
755 <https://doi.org/10.1016/j.apr.2018.08.011>, 2019.

756 Wong, J. P. S., Nenes, A., Weber, R. J. Changes in Light Absorptivity of Molecular
757 Weight Separated Brown Carbon Due to Photolytic Aging. *Environ. Sci.*
758 *Technol.*, 51, 8414–8421, <https://doi.org/10.1021/acs.est.7b01739>, 2017.

759 Wong, J. P. S., Tsagkaraki, M., Tsiodra, I., Mihalopoulos, N., Violaki, K., Kanakidou,
760 M., Sciare, J., Nenes, A., Weber, R. J. Effects of Atmospheric Processing on the
761 Oxidative Potential of Biomass Burning Organic Aerosols. *Environ. Sci.*
762 *Technol.*, 53, 6747–6756, <https://doi.org/10.1021/acs.est.9b01034>, 2019.

763 Yang, J., Au, W. C., Law, H., Lam, C. H., Nah, T. Formation and evolution of brown
764 carbon during aqueous-phase nitrate-mediated photooxidation of guaiacol and
765 5-nitroguaiacol. *Atmos. Environ.*, 254, 118401,
766 <https://doi.org/10.1016/j.atmosenv.2021.118401>, 2021.



- 767 Ye, Z., Hu, D., Wang, Z., Wang, H., Ge, X. Aqueous photochemical aging of
768 water-soluble smoke particles from crop straws burning. *Atmos. Environ.*, 340,
769 120879, <https://doi.org/10.1016/j.atmosenv.2024.120897>, 2025.
- 770 Ye, Z., Zhuang, Y., Chen, Y., Zhao, Z., Ma, S., Huang, H., Chen, Y., Ge, X.
771 Aqueous-phase oxidation of three phenolic compounds by hydroxyl radical:
772 Insight into secondary organic aerosol formation yields, mechanisms, products
773 and optical properties. *Atmos. Environ.*, 223, 117240,
774 <https://doi.org/10.1016/j.atmosenv.2019.117240>, 2020.
- 775 Zhang, B., Shen, Z., He, K., Sun, J., Huang, S., Xu, H., Li, J., Ho, S. S. H., Cao, J.
776 Insight into the Primary and Secondary Particle-Bound Methoxyphenols and
777 Nitroaromatic Compound Emissions from Solid Fuel Combustion and the
778 Updated Source Tracers. *Environ. Sci. Technol.*, 57, 14280-14288,
779 <https://doi.org/10.1021/acs.est.3c04370>, 2023.
- 780 Zhang, R., Gen, M., Liang, Z., Li, Y. J., Chan, C. K. Photochemical Reactions of
781 Glyoxal during Particulate Ammonium Nitrate Photolysis: Brown Carbon
782 Formation, Enhanced Glyoxal Decay, and Organic Phase Formation. *Environ.*
783 *Sci. Technol.*, 56, 1605-1614, <https://doi.org/10.1021/acs.est.1c07211>, 2022.
- 784 Zhao, R., Lee, A. K. Y., Huang, L., Li, X., Yang, F., Abbatt, J. P. D. Photochemical
785 processing of aqueous atmospheric brown carbon. *Atmos. Chem. Phys.*, 15,
786 6087-6100, <https://doi.org/10.5194/acp-15-6087-2015>, 2015.
- 787 Zhao, R., Zhang, Q., Xu, X., Wang, W., Zhao, W., Zhang, W., Zhang, Y. Effect of
788 photooxidation on size distribution, light absorption, and molecular compositions



789 of smoke particles from rice straw combustion. *Environ. Pollut.*, 311, 119950,
790 <https://doi.org/10.1016/j.envpol.2022.119950>, 2022.

791 Zheng, J., Hu, M., Du, Z., Shang, D., Gong, Z., Qin, Y., Fang, J., Gu, F., Li, M., Peng,
792 J., Li, J., Zhang, Y., Huang, X., He, L., Wu, Y., Guo, S. Influence of biomass
793 burning from South Asia at a high-altitude mountain receptor site in China.
794 *Atmos. Chem. Phys.*, 17, 6853-6864, <https://doi.org/10.5194/acp-17-6853-2017>,
795 2017.

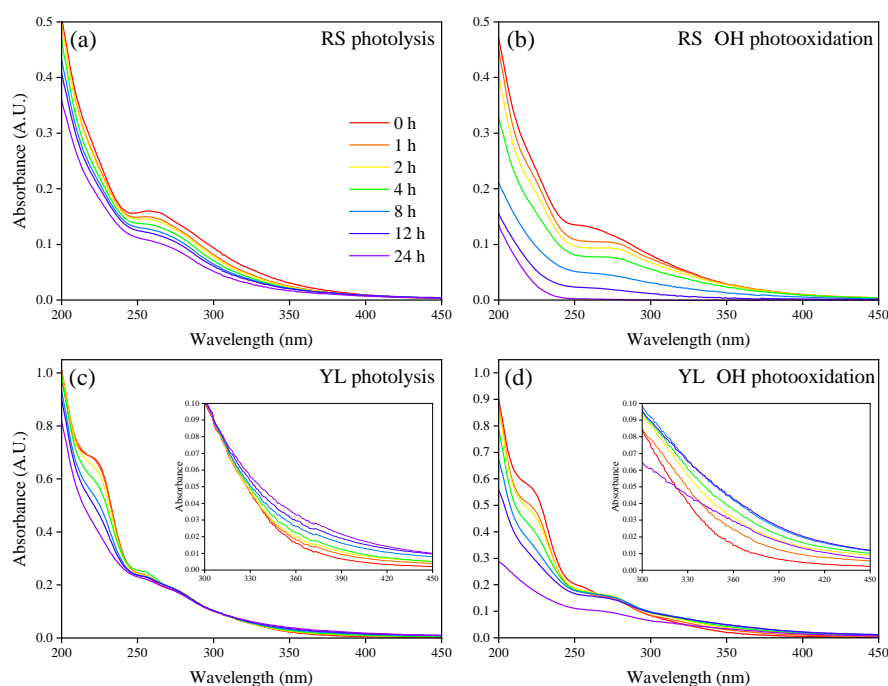
796 Zou, C., Cao, T., Li, M., Song, J., Jiang, B., Jia, W., Li, J., Ding, X., Yu, Z., Zhang, G.,
797 Peng, P. Measurement report: Changes in light absorption and molecular
798 composition of water-soluble humic-like substances during a winter haze
799 bloom-decay process in Guangzhou, China. *Atmos. Chem. Phys.*, 23, 963-979,
800 <https://doi.org/10.5194/acp-23-963-2023>, 2023.

801

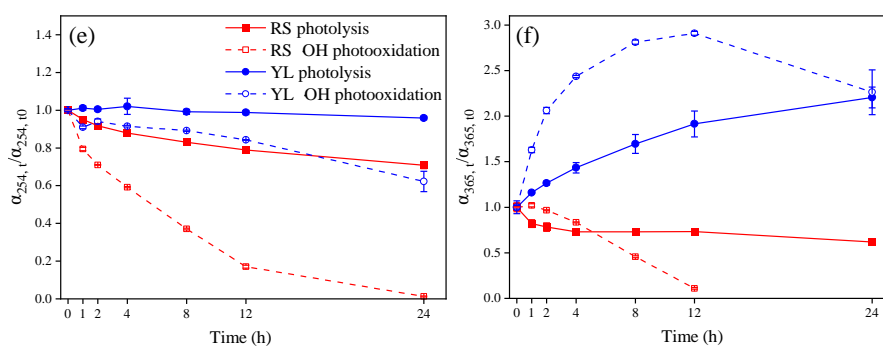
802



803



804



805

806 **Figure 1.** UV-vis spectra of RS and YL WSOM during photolysis (a and c) and OH
807 photooxidation (b and d) (The insert figure in c and d represent UV-vis spectra in wavelength
808 range 300–450 nm of YL WSOM during photolysis and OH photooxidation), and changes in
809 α_{254} (e) and α_{365} (f) of RS and YL WSOM during photolysis and OH photooxidation. The
810 error bars represent one standard deviation ($\pm 1\sigma$) of the triplicate samples.

811

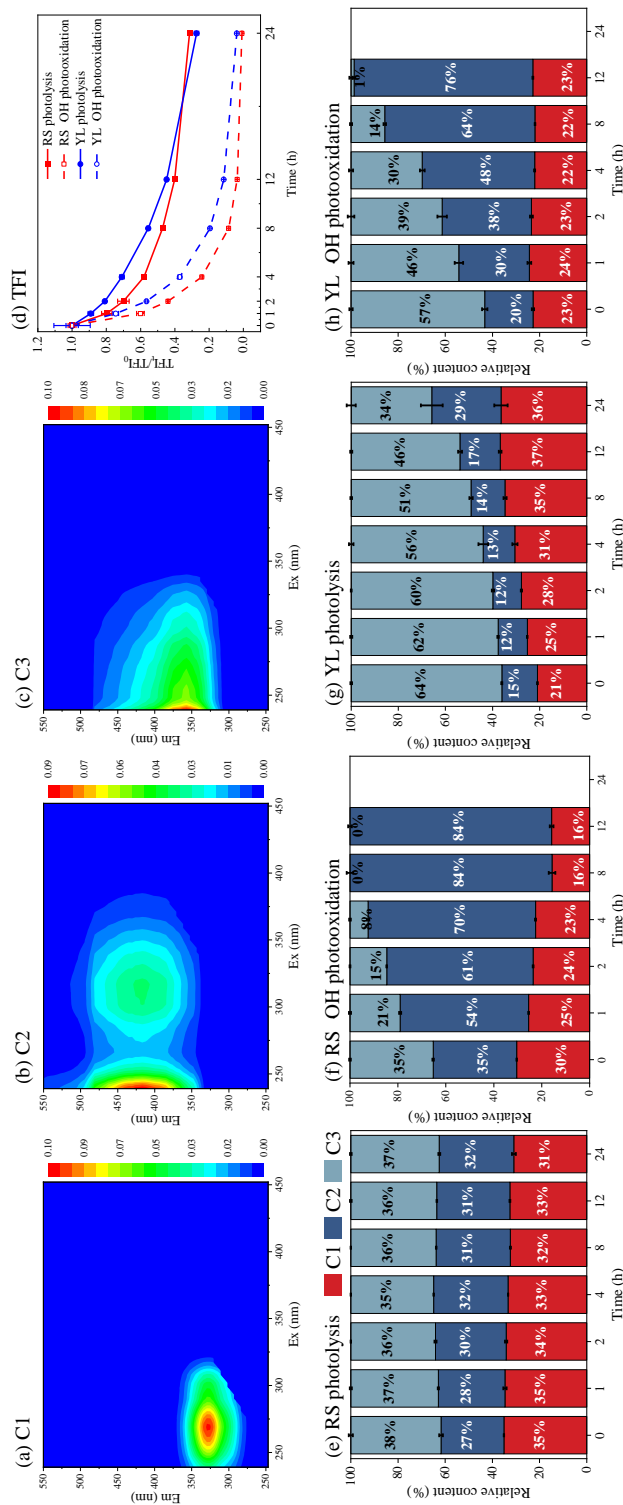


Figure 2. (a-c) EEM spectra of PARAFAC-derived fluorescence components (C1–C3) in RS and YL WSOM. Changes of total fluorescence intensity (TFI) (d) and the relative content of three individual fluorescence component within RS and YL WSOM during photolysis and OH photooxidation (e, f, g, h). The error bars represent one standard deviation ($\pm 1\sigma$) of the triplicate samples.

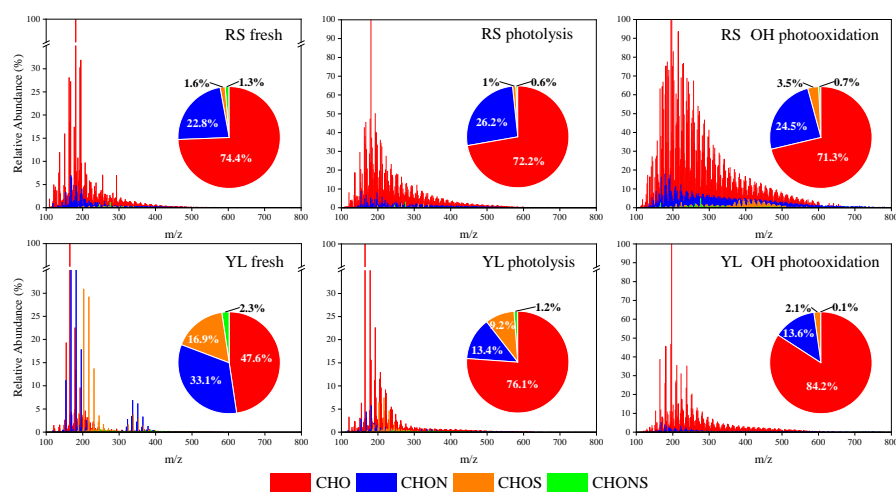


Figure 3. Reconstructed mass spectra of RS and YL WSOM for fresh (left), photolysis (middle) and OH photooxidation (right). Pie charts inserted represent the relative content of different formula groups in each sample by sum of intensities of all identified peaks.

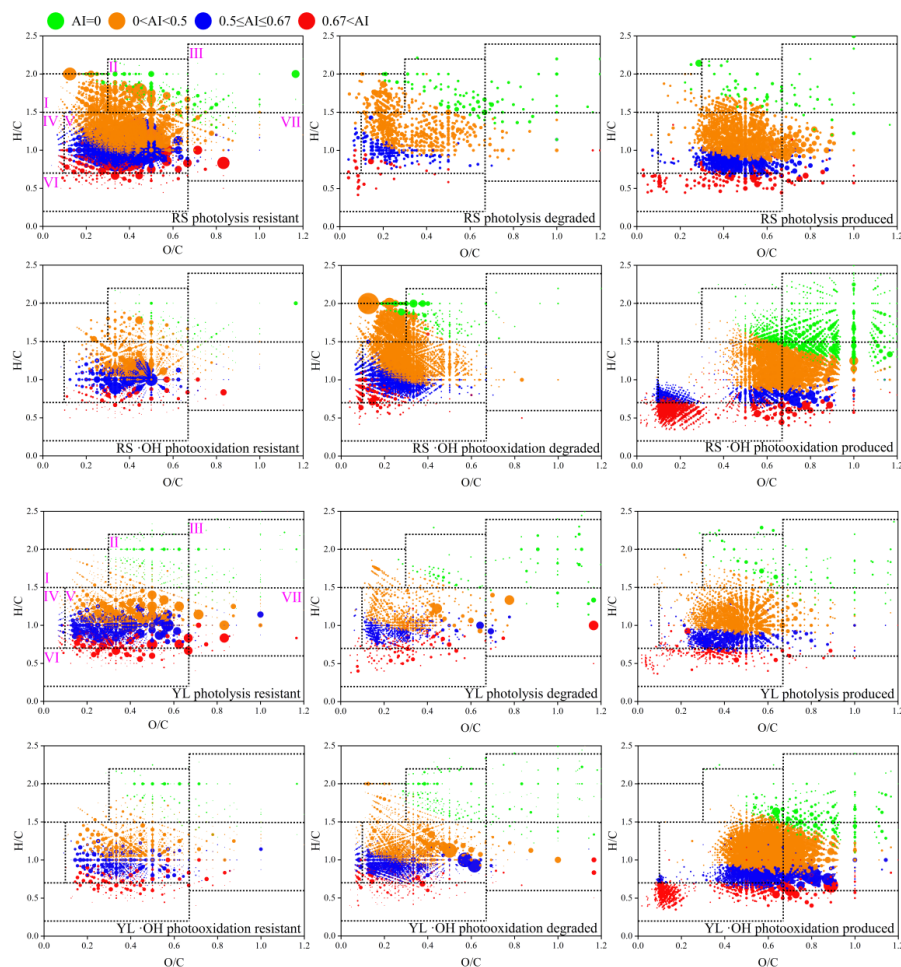


Figure 4. Van Krevelen diagrams for molecules resistant, degraded and produced after photolysis and OH photooxidation for RS WSOM (upper) and YL WSOM (bottom).